Article

# Leading hadronic contribution to the muon magnetic moment from lattice QCD

https://doi.org/10.1038/s41586-021-03418-1

Received: 2 August 2020

Accepted: 4 March 2021

Published online: 7 April 2021

Check for updates

Sz. Borsanyi[1], Z. Fodor[1,2,3,4,5]✉, J. N. Guenther[6,10], C. Hoelbling[1], S. D. Katz[4], L. Lellouch[7], T. Lippert[1,2], K. Miura[7,8,9], L. Parato[7], K. K. Szabo[1,2], F. Stokes[2], B. C. Toth[1], Cs. Torok[2] & L. Varnhorst[1,10]

The standard model of particle physics describes the vast majority of experiments and observations involving elementary particles. Any deviation from its predictions would be a sign of new, fundamental physics. One long-standing discrepancy concerns the anomalous magnetic moment of the muon, a measure of the magnetic field surrounding that particle. Standard-model predictions[1] exhibit disagreement with measurements[2] that is tightly scattered around 3.7 standard deviations. Today, theoretical and measurement errors are comparable; however, ongoing and planned experiments aim to reduce the measurement error by a factor of four. Theoretically, the dominant source of error is the leading-order hadronic vacuum polarization (LO-HVP) contribution. For the upcoming measurements, it is essential to evaluate the prediction for this contribution with independent methods and to reduce its uncertainties. The most precise, model-independent determinations so far rely on dispersive techniques, combined with measurements of the cross-section of electron–positron annihilation into hadrons[3–6]. To eliminate our reliance on these experiments, here we use ab initio quantum chromodynamics (QCD) and quantum electrodynamics simulations to compute the LO-HVP contribution. We reach sufficient precision to discriminate between the measurement of the anomalous magnetic moment of the muon and the predictions of dispersive methods. Our result favours the experimentally measured value over those obtained using the dispersion relation. Moreover, the methods used and developed in this work will enable further increased precision as more powerful computers become available.

The muon is an ephemeral sibling of the electron. It is 207 times more massive, but has the same electric charge and spin. Similarly to the electron, it behaves like a tiny magnet, characterized by a magnetic moment. This quantity is proportional to the spin and charge of the muon and inversely proportional to twice its mass. Dirac's relativistic quantum mechanics predicts that the constant of proportionality, $g_\mu$, should be equal to 2. However, in a relativistic quantum field theory such as the standard model, this prediction receives small corrections due to quantum vacuum fluctuations. These corrections are called the anomalous magnetic moment and are quantified by $(g_\mu - 2)/2$. They were measured to a precision of 0.54 ppm at the Brookhaven National Laboratory in the early 2000s[2], and have been calculated with a comparable precision (see ref. [7] for a recent review).

At this level of precision, all of the interactions of the standard model contribute. The leading contributions are electromagnetic and described by quantum electrodynamics (QED), but the one that dominates the theoretical error is induced by the strong interaction and requires solving the highly nonlinear equations of QCD at low energies. This contribution is determined by the LO-HVP, which describes how the propagation of a virtual photon is modified by the presence of quark and gluon fluctuations in the vacuum. Here we compute this LO-HVP contribution to $(g_\mu - 2)/2$, denoted by $a_\mu^{\text{LO-HVP}}$, using ab initio simulations in QCD and QED.

QCD is a generalized version of QED. The Euclidean Lagrangian for this theory is $\mathcal{L} = [1/(4e^2)]F_{\mu\nu}F_{\mu\nu} + [1/(2g^2)]\mathrm{tr}(G_{\mu\nu}G_{\mu\nu}) + \sum_f \bar{\psi}_f[\gamma_\mu(\partial_\mu + iq_fA_\mu + iB_\mu) + m_f]\psi_f$, where $\gamma_\mu$ are the Dirac matrices, $f$ runs over the 'flavours' of quarks, $m_f$ are the masses and the $q_f$ are the charges of quarks in units of the electron charge, $e$. Moreover, $F_{\mu\nu} = \partial_\mu A_\nu - \partial_\nu A_\mu$ and $G_{\mu\nu} = \partial_\mu B_\nu - \partial_\nu B_\mu + [B_\mu, B_\nu]$ and $g$ is the QCD coupling constant. In electrodynamics the gauge potential $A_\mu$ is a real-valued field, whereas in QCD $B_\mu$ is a $3 \times 3$ Hermitian matrix field. The different flavours of quarks are represented by independent fermionic fields, $\psi_f$. These fields have an additional 'colour' index in QCD, which runs from 1 to 3. In this work, we include both QED and QCD, as well as four non-degenerate quark flavours

[1]Department of Physics, University of Wuppertal, Wuppertal, Germany. [2]Jülich Supercomputing Centre, Forschungszentrum Jülich, Jülich, Germany. [3]Department of Physics, Pennsylvania State University, University Park, PA, USA. [4]Institute for Theoretical Physics, Eötvös University, Budapest, Hungary. [5]Department of Physics, University of California, San Diego, La Jolla, CA, USA. [6]Department of Physics, University of Regensburg, Regensburg, Germany. [7]Aix Marseille Université, Université de Toulon, CNRS, CPT, IPhU, Marseille, France. [8]Helmholtz Institute Mainz, Mainz, Germany. [9]Kobayashi-Maskawa Institute for the Origin of Particles and the Universe, Nagoya University, Nagoya, Japan. [10]Present address: Aix Marseille Université, Université de Toulon, CNRS, CPT, IPhU, Marseille, France. ✉e-mail: fodor@bodri.elte.hu

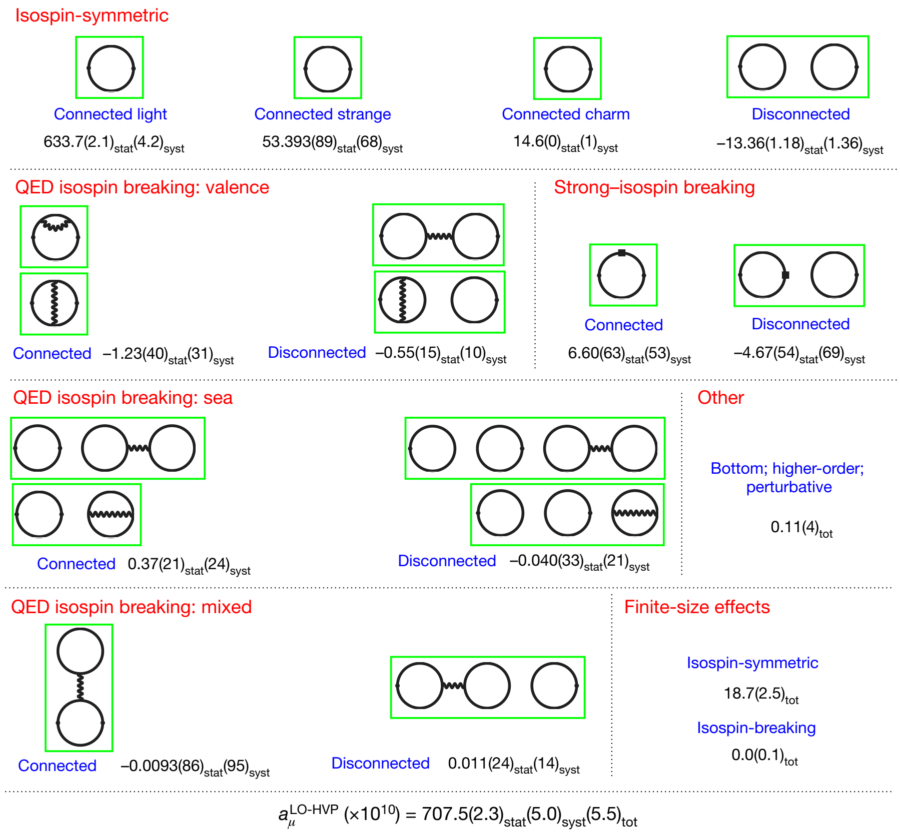


**Fig. 1 | Contributions to $a_\mu$, including examples of the corresponding Feynman diagrams.** Solid lines are quarks and curly lines are photons. Gluons are not shown explicitly, and internal quark loops are shown only if they are attached to photons. Dots represent coordinates in position space, boxes denote the mass insertion relevant for strong–isospin symmetry breaking. The numbers give our result for each contribution; they correspond to our 'reference' system size defined by $L_{\text{ref}} = 6.272$ fm spatial and $T_{\text{ref}} = 9.408$ fm temporal lattice extents. We also explicitly compute the finite-size corrections that must be added to these results, which are given separately in the lower right panel. The first error is the statistical and the second is the systematic uncertainty, except for the contributions for which only a single, total error is given. Central values are medians; errors are s.e.m.

(up, down, strange and charm), in a lattice formulation that takes into account all dynamical effects. We also consider the tiny contributions of the bottom and top quarks, as discussed in Supplementary Information.

We compute $a_\mu^{\text{LO-HVP}}$ in the so-called time–momentum representation[8], which relies on the following two-point function with zero three-momentum in Euclidean time $t$:

$$G(t) = \frac{1}{3e^2} \sum_{\mu=1,2,3} \int d^3x \langle J_\mu(\mathbf{x}, t) J_\mu(0) \rangle, \qquad (1)$$

where $J_\mu$ is the quark electromagnetic current, with $\frac{J_\mu}{e} = \frac{2}{3}\bar{u}\gamma_\mu u - \frac{1}{3}\bar{d}\gamma_\mu d - \frac{1}{3}\bar{s}\gamma_\mu s + \frac{2}{3}\bar{c}\gamma_\mu c$. $u, d, s$ and $c$ are the up, down, strange and charm quark fields, respectively, and the angle brackets stand for the QCD + QED expectation value to order $e^2$. It is convenient to decompose $G(t)$ into light, strange, charm and disconnected components, which have very different statistical and systematic uncertainties. Integrating the one-photon-irreducible part of the two-point function (equation (1)), $G_{1\gamma\text{I}}$, yields the LO-HVP contribution to the magnetic moment of the muon[8–11]:

$$a_\mu^{\text{LO-HVP}} = \alpha^2 \int_0^\infty dt K(t) G_{1\gamma\text{I}}(t), \qquad (2)$$

with weight function

$$K(t) = \int_0^\infty \frac{dQ^2}{m_\mu^2} \omega\left(\frac{Q^2}{m_\mu^2}\right)\left[t^2 - \frac{4}{Q^2}\sin^2\left(\frac{Qt}{2}\right)\right], \qquad (3)$$

and where $\omega(r) = [r + 2 - \sqrt{r(r+4)}\,]^2/\sqrt{r(r+4)}$, $\alpha$ is the fine-structure constant in the Thomson limit and $m_\mu$ is the muon mass. Because we consider only the LO-HVP contribution, for brevity we drop the superscript and multiply the result by $10^{10}$, that is, $a_\mu$ stands for $a_\mu^{\text{LO-HVP}} \times 10^{10}$ in the following.

The subpercent precision that we are aiming for represents a huge challenge for lattice QCD. To reach that goal, we must address four critical issues: scale determination; noise reduction; QED and strong–isospin symmetry breaking; and infinite-volume and continuum extrapolations. We discuss these one by one.

The first issue is scale determination. The quantity $a_\mu$ depends on the muon mass. When computing equation (2) on the lattice, $m_\mu$ must be converted into lattice units, $am_\mu$, where $a$ is the lattice spacing. A relative error of the lattice spacing propagates into about a twice-as-large relative error on $a_\mu$, so that $a$ must be determined with a precision of few parts per thousand. We use the mass of the $\Omega$ baryon, $M_\Omega = 1{,}672.45(29)$ MeV, from ref. [1] to set the lattice spacing, where the uncertainty in the parentheses denotes one standard deviation. We also use a scale based on the gradient flow from ref. [12], denoted as $w_0$, to define an isospin decomposition of our observables. Although $w_0$ can be determined with sub-per-thousand precision on the lattice, it is inaccessible experimentally. In this work we determine the physical value of $w_0$ by including QED and strong–isospin symmetry-breaking effects: $w_0 = 0.17236(29)_{\text{stat}}(63)_{\text{syst}}(70)_{\text{tot}}$ fm, where the first error is statistical, the second is systematic and the third is the total error. In total, we reach a relative accuracy of 4‰, which is better than the error of the previous best determination[13], the value of which agrees with ours. There the pion decay constant was used as experimental

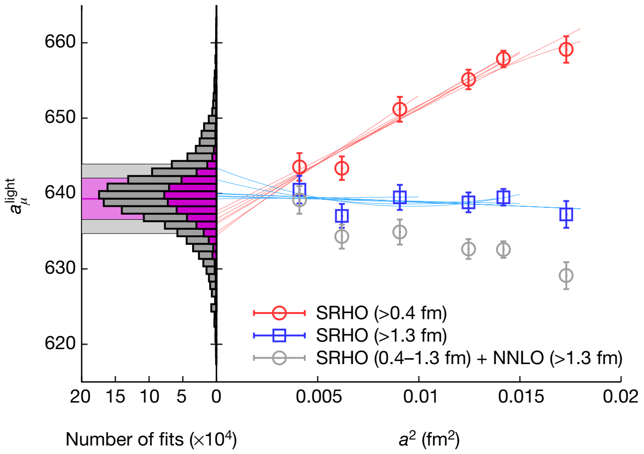


**Fig. 2 | Continuum extrapolation of the light connected component of $a_\mu$, $a_\mu^{\text{light}}$.** Before extrapolation we apply a taste-improvement procedure on the correlator, starting at some distance $t_{\text{sep}}$. (See Supplementary Information for details on the improvement 'SRHO'.) Datasets are shown for two choices of $t_{\text{sep}}$, 0.4 fm (red) and 1.3 fm (blue). The corresponding lines show fits using linear and quadratic terms of $a^2$ with varying number of lattice spacings in the fit. Our final analysis involves about 500,000 different continuum extrapolations, shown in the histogram on the left. The purple line in the left panel shows the central value of the final result. To estimate the error related to the taste-improvement procedure, we use next-to-next-to-leading-order staggered chiral perturbation theory (NNLO) in the long-distance part of the correlator ($t > 1.3$ fm). The corresponding data are shown with grey points, together with a histogram, from which the systematic error related to the taste improvement is obtained. The total error of the final result is given by the grey band in the left panel. Central values are medians; errors are s.e.m. The results are obtained on lattices of sizes $L \approx 6$ fm.

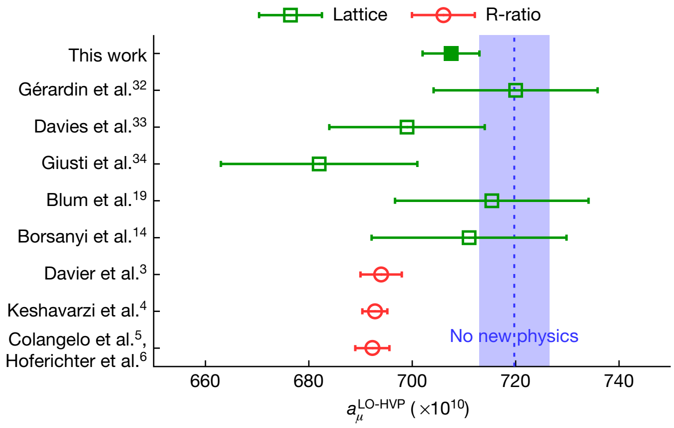


**Fig. 3 | Comparison of recent results for the LO-HPV contribution to the anomalous magnetic moment of the muon.** See ref. [7] for a recent review. Green squares are lattice results: this result (filled symbol) and those of Gérardin et al.[32], Davies et al.[33], Giusti et al.[34], Blum et al.[19] and our earlier work, Borsanyi et al.[14]. Central values are medians; error bars are s.e.m. Compared to Borsanyi et al.[14], this work has increased the accuracy of the scale setting from the per cent to the per thousand level; has decreased the statistical error from 7.5 to 2.3; has computed all isospin-symmetry-breaking contributions, as opposed to estimating it, with the corresponding error being 1.4, down from 5.1; has made a dedicated finite-size study to decrease the finite-size error from 13.5 to 2.5; has decreased the continuum extrapolation error from 8.0 to 4.1 by obtaining much more statistics on our finest lattice and applying taste improvement. Red circles were obtained using the R-ratio method by Davier et al.[3], Keshavarzi et al.[4], and Colangelo et al.[5] and Hoferichter et al.[6]; these results use the same experimental data as input. The blue shaded region is the value that $a_\mu^{\text{LO-HVP}}$ should have to explain the experimental measurement of $(g_\mu - 2)$, assuming no new physics.

input, and the isospin-symmetry-breaking effects were included only as an estimate.

The second issue is noise reduction. Our result for $a_\mu$ is obtained as an integral over the conserved current–current correlation function, from zero to infinite time separation, as shown in equation (2). For large separations the correlator is noisy, and this noise manifests itself as a statistical error in $a_\mu$. To reach the desired accuracy on $a_\mu$, one needs high precision at every step. Over 20,000 configurations were accumulated for our 27 ensembles on $L \approx 6$ fm lattices ($L$ is the spatial extent of the lattice). In addition, we include a lattice with $L \approx 11$ fm. The most important improvement over our earlier $a_\mu$ determination in ref. [14] is the extensive use of analysis techniques that are based on the lowest eigenmodes of the Dirac operator; see, for example, refs. [15–18]. An accuracy gain of about an order of magnitude can be reached using this technique for $a_\mu$ (refs. [19,20]).

The third issue is isospin-symmetry breaking. The precision needed cannot be reached with pure, isospin-symmetric QCD. Thus, we include QED effects and allow the up and down quarks to have different masses. These effects are included both in the scale determination and in the current–current correlators. We note that the separation of isospin-symmetric and isospin-symmetry-breaking contributions requires a convention, which we discuss in detail in Supplementary Information. Strong–isospin breaking is implemented by taking derivatives of QCD + QED expectation values with respect to up/down quark masses and computing the resulting observables on isospin-symmetric configurations[21]. We note that the first derivative of the fermionic determinant vanishes. We also implement derivatives with respect to the electric charge[22]. It is useful to distinguish between the electric charge in the fermionic determinant ($e_s$ or sea electric charge) and in the observables ($e_v$ or valence electric charge). The complete list of graphs that should be evaluated are shown in Fig. 1 with our numerical results for them.

The final observable is given as a Taylor expansion around the isospin-symmetric, physical-mass point with zero sea and valence charges. Instead of the quark masses, we use the pseudoscalar meson masses of pions and kaons, which can be determined with high precision. Using the expansion coefficients, we extrapolate in the charges, in the strong–isospin symmetry-breaking parameter and in the lattice spacing, and interpolate in the quark masses to the physical point. Thus, we obtain $a_\mu$ and its statistical and systematic uncertainties.

The fourth issue is the extrapolation to the infinite-volume and continuum limit. The standard wisdom for lattice calculations is that $M_\pi L > 4$ should be taken, where $M_\pi$ is the mass of the pion. Unfortunately, this is not satisfactory in the present case: $a_\mu$ is far more sensitive to $L$ than other quantities, such as hadron masses, and large volumes are needed to reach per-thousand accuracy. For less volume-sensitive quantities, we use well established results to determine the finite-volume corrections on the pion decay constant[23] and on charged hadron masses[24–26]. Leading-order chiral perturbation theory[27] and two-loop, partially quenched chiral perturbation theory[20,28] for $a_\mu$ help to describe finite-size corrections, but the non-perturbative, leading-order, large-$L$ expansion of ref. [29] indicates that those approaches still lead to systematic effects that are larger than the accuracy that we are aiming for. In addition to the infinite-volume extrapolation, the continuum extrapolation is also difficult. This is connected to the taste-symmetry breaking of staggered fermions, which we use in this work.

We correct for finite-volume effects on $a_\mu$ by computing them directly by performing lattice simulations on $L \approx 11$ fm lattices, with highly suppressed taste violations and with physical, taste-averaged pion masses. These corrections are cross-checked against three models that describe the relevant long-distance physics, in turn validating the use of these models for the residual, sub-per-thousand extrapolation to infinite volume. These models include: (i) the full two-loop, finite-volume, chiral perturbation theory corrections for $a_\mu$; (ii) the

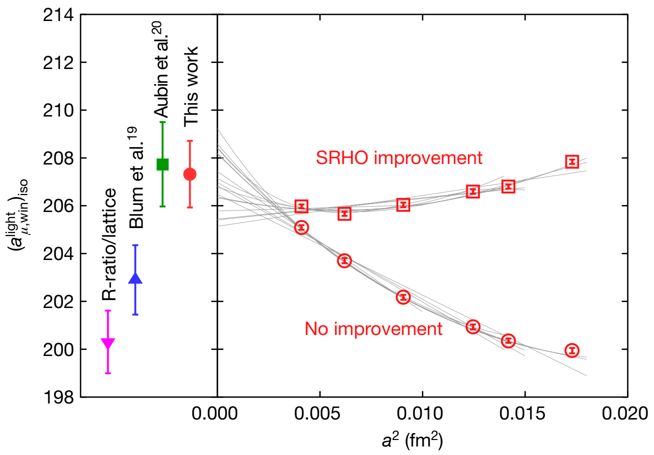


**Fig. 4 | Continuum extrapolation of the isospin-symmetric, light, connected component of the window observable $a_{\mu,\text{win}}$, $(a^{\text{light}}_{\mu,\text{win}})_{\text{iso}}$.** The data points are extrapolated to the infinite-volume limit. Central values are medians; error bars are s.e.m. Two different ways to perform the continuum extrapolations are shown: one without improvement, and another with corrections from a model involving the $\rho$ meson (SRHO). In both cases the lines show linear, quadratic and cubic fits in $a^2$ with varying number of lattice spacings in the fit. The continuum-extrapolated result is shown with the results from Blum et al.[19] and Aubin et al.[20]. Also plotted is our R-ratio-based determination, obtained using the experimental data compiled by the authors of ref. [4] and our lattice results for the non-light-connected contributions. This plot is convenient for comparing different lattice results. Regarding the total $a_{\mu,\text{win}}$, for which we must also include the contributions of flavours other than light and isospin-symmetry-breaking effects, we obtain $236.7(1.4)_{\text{tot}}$ on the lattice and $229.7(1.3)_{\text{tot}}$ from the R-ratio; the latter is $3.7\sigma$ or 3.1% smaller than the lattice result.

Meyer–Lellouch–Lüscher–Gounaris–Sakurai technique described in Supplementary Information; and (iii). the $\rho$–$\pi$–$\gamma$ model of Jegerlehner and Szafron[30], already used in a lattice context in ref. [31]. Moreover, to reduce discretization errors in the light-quark contributions to $a_\mu$, before extrapolating those contributions to the continuum, we apply a taste-improvement procedure that reduces lattice artefacts due to taste-symmetry breaking. The procedure is built upon the three models of $\pi$–$\rho$ physics mentioned above. We provide evidence that validates this procedure in Supplementary Information.

Combining all of these ingredients, we obtain as a final result $a_\mu = 707.5(2.3)_{\text{stat}}(5.0)_{\text{syst}}(5.5)_{\text{tot}}$. The statistical error comes mainly from the noisy, large-distance region of the current–current correlator. The systematic error is dominated by the continuum extrapolation and the finite-size effect computation. The total error is obtained by adding the first two in quadrature. In total, we reach a relative accuracy of 0.8%. In Fig. 2 we show the continuum extrapolation of the light, connected component of $a_\mu$, which gives the dominant contribution to $a_\mu$.

Figure 3 compares our result with previous lattice computations and also with results from the R-ratio method, which have recently been reviewed in ref. [7]. In principle, one can reduce the uncertainty of our result by combining our lattice correlator, $G(t)$, with the one obtained from the R-ratio method, in regions of Euclidean time in which the latter is more precise[19]. We do not do so here because there is a tension between our result and those obtained by the R-ratio method, as can be seen in Fig. 3. For the total LO-HVP contribution to $a_\mu$, our result is $2.0\sigma$, $2.5\sigma$, $2.4\sigma$ and $2.2\sigma$ larger than the R-ratio results of $a_\mu = 694.0(4.0)$ (ref. [3]), $a_\mu = 692.78(2.42)$ (ref. [4]), $a_\mu = 692.3(3.3)$ (refs. [5,6]) and the combined result $a_\mu = 693.1(4.0)$ of ref. [7], respectively. It is worth noting that the R-ratio determinations are based on the same experimental datasets and are therefore strongly correlated, although these datasets were obtained in several different and independent experiments that we have no reason to believe are collectively biased. Clearly, these comparisons need further investigation, although it should also be kept in mind that the tensions observed here are smaller, for instance, than what is usually considered experimental evidence for a new phenomenon ($3\sigma$) and much smaller than what is needed to claim an experimental discovery ($5\sigma$).

As a first step in that direction, it is instructive to consider a modified observable, where the correlator $G(t)$ is restricted to a finite interval by a smooth window function[19]. This observable, which we denote as $a_{\mu,\text{win}}$, is obtained much more readily than $a_\mu$ on the lattice. Its shorter-distance nature makes it far less susceptible to statistical noise and to finite-volume effects. Moreover, in the case of staggered fermions, it has reduced discretization artefacts. This is shown in Fig. 4, where the light, connected component of $a_{\mu,\text{win}}$ is plotted as a function of $a^2$. Because the determination of this quantity does not require overcoming many of the challenges described above, other lattice groups have obtained it with errors comparable to ours[19,20]. This allows a sharper benchmarking of our calculation of this challenging, light-quark contribution that dominates $a_\mu$. Our $a^{\text{light}}_{\mu,\text{win}}$ differs by $0.2\sigma$ and $2.2\sigma$ from the lattice results of ref. [20] and ref. [19], respectively. Moreover, $a_{\mu,\text{win}}$ can be computed using the R-ratio approach, and we do so using the dataset provided by the authors of ref. [4]. However, here we find a $3.7\sigma$ tension with our lattice result.

To conclude, when combined with the other standard-model contributions (see, for example, refs. [3,4]), our result for the leading-order hadronic contribution to the anomalous magnetic moment of the muon, $a_\mu^{\text{LO-HVP}} = 707.5(5.5)_{\text{tot}} \times 10^{-10}$, weakens the long-standing discrepancy between experiment and theory. However, as discussed above and can be seen in Fig. 2, our lattice result shows some tension with the R-ratio determinations of refs. [3–6]. Obviously, our findings should be confirmed—or refuted—by other studies using different discretizations of QCD. Those investigations are underway.

## Online content

Any methods, additional references, Nature Research reporting summaries, source data, extended data, supplementary information, acknowledgements, peer review information; details of author contributions and competing interests; and statements of data and code availability are available at https://doi.org/10.1038/s41586-021-03418-1.


1. Tanabashi, M. et al. Review of particle physics. *Phys. Rev. D* **98**, 030001 (2018).
2. Bennett, G. W. et al. Final report of the muon E821 anomalous magnetic moment measurement at BNL. *Phys. Rev. D* **73**, 072003 (2006).
3. Davier, M., Hoecker, A., Malaescu, B. & Zhang, Z. A new evaluation of the hadronic vacuum polarisation contributions to the muon anomalous magnetic moment and to $\alpha(m_Z^2)$. *Eur. Phys. J. C* **80**, 241 (2020); erratum **80**, 410 (2020).
4. Keshavarzi, A., Nomura, D. & Teubner, T. $g-2$ of charged leptons, $\alpha(M_Z^2)$, and the hyperfine splitting of muonium. *Phys. Rev. D* **101**, 014029 (2020).
5. Colangelo, G., Hoferichter, M. & Stoffer, P. Two-pion contribution to hadronic vacuum polarization. *J. High Energy Phys.* **2019**, 006 (2019).
6. Hoferichter, M., Hoid, B. L. & Kubis, B. Three-pion contribution to hadronic vacuum polarization. *J. High Energy Phys.* **2019**, 137 (2019).
7. Aoyama, T. et al. The anomalous magnetic moment of the muon in the Standard Model. *Phys. Rep.* **887**, 1–166 (2020).
8. Bernecker, D. & Meyer, H. B. Vector correlators in lattice QCD: methods and applications. *Eur. Phys. J. A* **47**, 148 (2011).
9. Lautrup, B. E., Peterman, A. & de Rafael, E. Recent developments in the comparison between theory and experiments in quantum electrodynamics. *Phys. Rep.* **3**, 193–259 (1972).
10. de Rafael, E. Hadronic contributions to the muon g–2 and low-energy QCD. *Phys. Lett. B* **322**, 239–246 (1994).
11. Blum, T. Lattice calculation of the lowest order hadronic contribution to the muon anomalous magnetic moment. *Phys. Rev. Lett.* **91**, 052001 (2003).
12. Borsanyi, S. et al. High-precision scale setting in lattice QCD. *J. High Energy Phys.* **2012**, 010 (2012).
13. Dowdall, R. J., Davies, C. T. H., Lepage, G. P. & McNeile, C. $V_{us}$ from $\pi$ and $K$ decay constants in full lattice QCD with physical $u$, $d$, $s$ and $c$ quarks. *Phys. Rev. D* **88**, 074504 (2013).
14. Borsanyi, S. et al. Hadronic vacuum polarization contribution to the anomalous magnetic moments of leptons from first principles. *Phys. Rev. Lett.* **121**, 022002 (2018).

15. Neff, H., Eicker, N., Lippert, T., Negele, J. W. & Schilling, K. On the low fermionic eigenmode dominance in QCD on the lattice. *Phys. Rev. D* **64**, 114509 (2001).
16. Giusti, L., Hernandez, P., Laine, M., Weisz, P. & Wittig, H. Low-energy couplings of QCD from current correlators near the chiral limit. *J. High Energy Phys*. **2004**, 013 (2004).
17. DeGrand, T. A. & Schaefer, S. Improving meson two point functions in lattice QCD. *Comput. Phys. Commun*. **159**, 185–191 (2004).
18. Shintani, E. et al. Covariant approximation averaging. *Phys. Rev. D* **91**, 114511 (2015).
19. Blum, T. et al. Calculation of the hadronic vacuum polarization contribution to the muon anomalous magnetic moment. *Phys. Rev. Lett*. **121**, 022003 (2018).
20. Aubin, C. et al. Light quark vacuum polarization at the physical point and contribution to the muon $g-2$. *Phys. Rev. D* **101**, 014503 (2020).
21. de Divitiis, G. M. et al. Isospin breaking effects due to the up-down mass difference in Lattice QCD. *J. High Energy Phys*. **2012**, 124 (2012).
22. de Divitiis, G. M. et al. Leading isospin breaking effects on the lattice. *Phys. Rev. D* **87**, 114505 (2013).
23. Colangelo, G., Durr, S. & Haefeli, C. Finite volume effects for meson masses and decay constants. *Nucl. Phys. B* **721**, 136–174 (2005).
24. Davoudi, Z. & Savage, M. J. Finite-volume electromagnetic corrections to the masses of mesons, baryons and nuclei. *Phys. Rev. D* **90**, 054503 (2014).
25. Borsanyi, S. et al. Ab initio calculation of the neutron-proton mass difference. *Science* **347**, 1452–1455 (2015).
26. Fodor, Z. et al. Quantum electrodynamics in finite volume and nonrelativistic effective field theories. *Phys. Lett. B* **755**, 245–248 (2016).
27. Aubin, C. et al. Finite-volume effects in the muon anomalous magnetic moment on the lattice. *Phys. Rev. D* **93**, 054508 (2016).
28. Bijnens, J. & Relefors, J. Vector two-point functions in finite volume using partially quenched chiral perturbation theory at two loops. *J. High Energy Phys*. **2017**, 114 (2017).
29. Hansen, M. T. & Patella, A. Finite-volume effects in $(g-2)_\mu^{\mathrm{HVP,LO}}$. *Phys. Rev. Lett*. **123**, 172001 (2019).
30. Jegerlehner, F. & Szafron, R. $\rho^0-\gamma$ mixing in the neutral channel pion form factor $F_\pi^e$ and its role in comparing $e^+e-$ with $\tau$ spectral functions. *Eur. Phys. J. C* **71**, 1632 (2011).
31. Chakraborty, B. et al. The hadronic vacuum polarization contribution to $a_\mu$ from full lattice QCD. *Phys. Rev. D* **96**, 034516 (2017).
32. Gérardin, A. et al. The leading hadronic contribution to $(g-2)_\mu$ from lattice QCD with $N_f = 2+1$ flavours of O($a$) improved Wilson quarks. *Phys. Rev. D* **100**, 014510 (2019).
33. Davies, C. T. H. et al. Hadronic-vacuum-polarization contribution to the muon's anomalous magnetic moment from four-flavor lattice QCD. *Phys. Rev. D* **101**, 034512 (2020).
34. Giusti, D., Lubicz, V., Martinelli, G., Sanfilippo, F. & Simula, S. Electromagnetic and strong isospin-breaking corrections to the muon $g-2$ from Lattice QCD+QED. *Phys. Rev. D* **99**, 114502 (2019).

# Methods

### Finite-size effects

Finite-size effects on $a_\mu$ were the largest source of uncertainty in our previous work[14]. We compute these effects in a systematic way, which includes dedicated lattice simulations, chiral perturbation theory (XPT) and phenomenological models. The goal is to provide a single number that is to be added to the continuum-extrapolated lattice result obtained in a reference box, which is defined by a spatial extent of $L_{\rm ref} = 6.272$ fm and a temporal extent of $T_{\rm ref} = (3/2)L_{\rm ref}$. Here we summarize our findings on the finite-size effect of the isospin-symmetric part. More details and a discussion of the isospin-symmetry-breaking part can be found in Supplementary Information.

We perform dedicated lattice simulations with two different lattice geometries: one is a $56 \times 84$ lattice with the reference box size and the other is a large $96 \times 96$ lattice with box size $L = L_{\rm big} = 10.752$ fm and $T = T_{\rm big} = L_{\rm big}$. Because taste violations distort the finite-size effects, we designed a new action with highly suppressed taste breaking, which we call 4HEX. Our strategy is then to compute the finite-size correction as the following sum:

$$\begin{aligned} a_\mu(\infty,\infty) - a_\mu(L_{\rm ref}, T_{\rm ref}) &= [a_\mu(L_{\rm big}, T_{\rm big}) - a_\mu(L_{\rm ref}, T_{\rm ref})]_{\rm 4HEX} \\ &\quad + [a_\mu(\infty,\infty) - a_\mu(L_{\rm big}, T_{\rm big})]_{\rm XPT}. \end{aligned} \tag{4}$$

The first difference on the right-hand side is taken from the dedicated 4HEX simulations. The second difference is expected to be much smaller than the first, and is taken from a non-lattice approach: two-loop XPT.

We consider four non-lattice approaches to compute both differences on the right-hand side of equation (4). In the case of the first difference, the results obtained are compared to our 4HEX simulations. The first approach is XPT to next-to-leading order (NLO) and next-to-next-to-leading order (NNLO), the second is the Meyer–Lellouch–Lüscher–Gounaris–Sakurai (MLLGS) model, the third approach is that of Hansen and Patella (HP)[29] and the fourth is the $\rho$–$\pi$–$\gamma$ (RHO) model of ref. [31].

We compute the first difference in equation (4) using dedicated simulations with the 4HEX action. We use the harmonic mean square (HMS) to set the physical point:

$$M_{\pi,\rm HMS}^{-2} \equiv \frac{1}{16}\sum_\alpha M_{\pi,\alpha}^{-2}$$

defined as an average over the masses of the 16 pion tastes, $M_{\pi,\alpha}$. We set $M_{\pi,\rm HMS}$ to the physical value of the pion mass, which requires lowering the Goldstone pion mass to 110 MeV. This way of fixing the physical point results in much smaller lattice artefacts than the usual setting with the Goldstone pion, at least for an observable such as the finite-size effect.

To generate the 4HEX dataset, we performed simulations with two different Goldstone pion masses: $M_\pi = 104$ MeV and 121 MeV. To set the physical point as described above, we performed an interpolation from these two pion masses to $M_\pi = 110$ MeV.

To compute $a_\mu^{\rm light}$ from the current propagator in our 4HEX simulations, we use the upper- and lower-bound technique described in Supplementary Information. Results for the $M_\pi = 121$ MeV simulation point are plotted in Extended Data Fig. 1. The bounds meet at around 4.2 fm and 4.7 fm on the small and large volumes, respectively. At these distances, we take the average of the two bounds as an estimate for $a_\mu^{\rm light}$. The results are given in Extended Data Table 1.

We have only one lattice spacing with the 4HEX action, so the finite-size effects cannot be extrapolated to the continuum limit. We estimate the cutoff effect of the result by comparing the total $a_\mu$ with the 4HEX action at this single lattice spacing to the continuum-extrapolated *4stout* action-based lattice result, both in the $L_{\rm ref}$ volume. The 4HEX result is about 7% larger than the continuum value. Therefore, we reduce the measured finite-size effect by 7%, and assign a 7% uncertainty to this correction step. For the difference we get:

$$a_\mu(L_{\rm big}, T_{\rm big}) - a_\mu(L_{\rm ref}, T_{\rm ref}) = 18.1(2.0)_{\rm stat}(1.4)_{\rm cont}. \tag{5}$$

The result is obtained from the $a_\mu^{\rm light}$ numbers of Extended Data Table 1, including a (9/10) charge factor. The first error is statistical and the second is an estimate of the cutoff effect.

Extended Data Table 2 collects the finite-size effect computed in various non-lattice approaches. The different models give finite-size effects of similar size, which agree well with the lattice determination of equation (5). Only the NLO result differs by about $3\sigma$. The fact that NLO XPT underestimates the finite-size effect was shown in ref. [35], at a non-physical pion mass. Using the physical pion mass, a dedicated finite-volume study was presented in ref. [36]; it reaches the same conclusion as we do, albeit with larger errors. We also see that, according to the models, the finite-$T$ effect is much smaller than the finite-$L$ effect.

The good agreement for the finite-size effect of the reference box between the models and the lattice gives us confidence that the models can be used to reliably compute the very small, residual, finite-size effect of the large box. The corresponding model estimates can be found in Extended Data Table 1. For an infinite-time extent, the NNLO XPT, HP and RHO approaches agree nicely. As a final value for the large-box, finite-size effect we take the NNLO XPT result including finite-$T$ effects:

$$a_\mu(\infty,\infty) - a_\mu(L_{\rm big}, T_{\rm big}) = 0.6(0.3)_{\rm big},$$

where the uncertainty is an estimate of higher-order effects, given here by the difference of the NNLO and NLO values.

For our final result for the finite-size effect of the reference box, we also include the contribution of isoscalar channel and isospin-symmetry-breaking effects, giving:

$$\begin{aligned} &a_\mu(\infty,\infty) - a_\mu(L_{\rm ref}, T_{\rm ref}) \\ &\quad = 18.7(2.0)_{\rm stat}(1.4)_{\rm cont}(0.3)_{\rm big}(0.6)_{I=0}(0.1)_{\rm qed}(2.5)_{\rm tot}. \end{aligned}$$

The first error is the statistical uncertainty of our 4HEX computation, the second is an estimate of the 4HEX cutoff effects, the third is the uncertainty of the residual finite-size effect of the 'big' lattice, the fourth is an XPT estimate of the isoscalar (isospin $I = 0$) finite-size effect and the fifth is an estimate of the isospin-symmetry-breaking effects. The last, total error is the sum of the first five, added in quadrature. The vast majority of the finite-size effects is obtained using the 4HEX lattice computation; for the rest we apply analytical methods that are validated by the lattice computation: for the main contribution they give values that are consistent with the lattice result.

### Taste improvement

As is well known, some of the most important cutoff effects of staggered fermions are taste violations. At long distances, these violations distort the pion spectrum. Because $a_\mu$ is predominantly a long-distance observable, dominated by a two-pion contribution, including the $\rho$ resonance, we expect these effects to be largest in the light-quark terms.

We investigate various physically motivated models for reducing long-distance taste violations in our lattice results. We consider three techniques: NNLO XPT, the MLLGS model and the RHO model. For the definition of these models, see Supplementary Information. We investigate and discuss the suitability of their staggered versions for reducing the taste violations present in our lattice data. We call the resulting corrections taste improvements, because they improve the continuum extrapolation of our lattice data without, in principle, modifying the continuum-limit value. Indeed, these corrections vanish in that limit, as taste-symmetry-breaking effects should. These improvements are applied on light-quark observables at the isospin-symmetric point, the taste violations of which have the largest impact on our final uncertainties.

The NNLO XPT, MLLGS and RHO models describe the long-distance physics associated with finite-volume effects, as measured in our simulations. One can also define corresponding models that describe the taste violations, denoted as NNLO SXPT, SMLLGS and SRHO, respectively. We find that these describe the physics associated with taste violations, at least at larger distances. This is illustrated in Extended Data Fig. 2, where cutoff effects in the integrand of $a_\mu^{\rm light}$ are plotted as a function of Euclidean time. More specifically, we define the physical observable obtained by convoluting the integrand of $a_\mu^{\rm light}$ with a smooth window function $W(t; t_1)$ of a width of 0.5 fm and starting at a time of $t_1$. Then we consider the difference in the value of this observable, obtained on a fine and a coarse lattice at a sequence of $t_1$ values separated by 0.1 fm. These are compared to the NLO SXPT, NNLO SXPT, SRHO and SMLLGS predictions for this quantity, evaluated at the exact parameters of the ensembles.

The SMLLGS, SRHO and NNLO SXPT taste improvements describe the numerical data very nicely for $t_1 \gtrsim 2.0$ fm, fairly well for $t_1 \gtrsim 1.0$ fm and all the way down to $t_1 \approx 0.4$ fm in the case of SRHO. All three slightly overestimate the observed cutoff effects, with the $\rho$-meson-based approach performing best, whereas NNLO displays a large deviation from the lattice results in the $t_1 \leq 0.8$ fm region. The lattice results have a maximum at $t_1 = 1.4$ fm, as does the SRHO improvement, reinforcing our confidence that this model captures the relevant physics.

These findings lead us to apply the following taste corrections to our simulation results for $a_\mu^{\rm light}(L, T, a)$, obtained on an $L^3 \times T$ lattice with lattice spacing $a$, before performing continuum extrapolations:

$$a_\mu^{\rm light}(L,T,a) \to a_\mu^{\rm light}(L,T,a) + \frac{10}{9}\left[a_{\mu,t\geq t_{\rm sep}}^{\rm RHO}(L_{\rm ref}, T_{\rm ref}) - a_{\mu,t\geq t_{\rm sep}}^{\rm SRHO}(L,T,a)\right],$$

with $t_{\rm sep} = 0.4$, 0.7, 1.0 and 1.3 fm, and where the factor (10/9) is related to the quark charges. We note that by using $L_{\rm ref}$ and $T_{\rm ref}$ in the above equation, we apply a very small volume correction to interpolate all of our simulation results to the same reference four-volume, so that they can be extrapolated to the continuum limit together.

The taste-improved data are then extrapolated to the continuum using our standard fitting procedure, in the course of which isospin-symmetry-breaking effects are also included. To estimate the systematic error we use a histogram technique. The central values and the detailed error budget of this analysis can be found in Supplementary Information.

The procedure described above does not yet take into account the systematic uncertainty associated with our choice of SRHO for taste improvement for $t > 1.3$ fm. Given that applying no taste improvement in that region is not an option, because of the nonlinearities introduced by two-pion taste violations, we turn to NNLO SXPT, only as a means of estimating the uncertainty associated with this choice. Thus, we define this systematic uncertainty as ERR = (SRHO − NNLO SXPT) for $t > 1.3$ fm. Then, we perform the same histogram analysis but with SRHO, SRHO − ERR and SRHO + ERR improvements. From this histogram we extract the contribution that comes from the variation in the improvement model from SRHO − ERR to SRHO + ERR. We assign this full spread to the systematic uncertainty associated with the taste-improvement procedure. We add this error in quadrature to the error given by the histogram technique discussed in the previous paragraph.

The procedure is illustrated in Extended Data Fig. 3, which shows the datasets for $a_\mu^{\rm light}$ without and with taste improvements, as functions of $a^2$. (See also Fig. 2, which zooms in on the taste-improved, continuum extrapolations.) The SRHO improvements with $t_{\rm sep} = 0.4$ fm are shown as red points, whereas blue points correspond to $t_{\rm sep} = 1.3$ fm. These plots include isospin-symmetry-breaking contributions. An example of our lattice results with SRHO improvement between $t = 0.4$ fm and $t = 1.3$ fm and NNLO SXPT improvement are shown as grey points in Extended Data Fig. 3.

An important check of our taste-improvement procedure is provided by the study of the isoscalar or $I = 0$ contribution to $a_\mu$, as suggested by arguments made in ref. [32]. Here we work with the isospin-symmetric datasets. Then the $I = 0$ contribution is defined as:

$$a_\mu^{I=0} \equiv \frac{1}{10} a_\mu^{\rm light} + a_\mu^{\rm disc} + \cdots, \tag{6}$$

where the ellipsis stands for the quark-connected contributions of the more massive $s, c, \ldots$ quarks. This quantity receives no two-pion contributions: it starts with three pions, the taste-symmetry-breaking effects of which should be very small. Thus, if our understanding of discretization errors in $a_\mu^{\rm light}$ and $a_\mu^{\rm disc}$ is correct, the taste-symmetry-breaking corrections observed in the light and disconnected quantities must be largely absent from $a_\mu^{I=0}$. As a consequence, we expect the continuum extrapolation of $a_\mu^{I=0}$ to be much milder. That is exactly what is shown in Extended Data Fig. 4 and explained in its caption.

**Results for $w_0$, $M_{ss}$ and $\Delta M^2$**

Here we describe the details of the analyses that are used to obtain the physical values of $w_0$, $M_{ss}$ and $\Delta M^2 = M_{dd}^2 - M_{uu}^2$ from the experimental values of hadron masses, including the mass of the $\Omega$ baryon. $M_{uu}$, $M_{dd}$ and $M_{ss}$ denote the masses of mesons built from an up and an anti-up, a down and an anti-down, and a strange and an anti-strange quark, respectively, without quark-disconnected contributions. The results for these quantities are used to define the isopin-symmetric point in this work, as described in Supplementary Information.

In the case of $w_0$, the observable that we fit is $w_0 M_\Omega$. To account for the systematic error due to the different continuum extrapolations, we apply both linear and quadratic functions in the isospin-symmetric component. We also remove zero/one/two/three of the coarsest lattice spacings in the linear fit and zero/one/two lattice spacings in the quadratic fit. For the tiny valence QED component only linear fits are applied, with zero/one/two points removed; for the even smaller sea QED contributions, we have either a constant or a linear fit with all lattice spacings.

The systematic error of the hadron mass fits is taken into account by 24 different combinations of the fit ranges: three for the $M_\Omega$ mass, two for the pseudoscalars, two for the isospin breaking of the $M_\Omega$, and two for the isospin breaking of the pseudoscalars. To account for the experimental error on $M_\Omega$, we carry out the analysis with two different experimental values: one that corresponds to the central value plus the experimental error, and another with this error subtracted.

Altogether, these yield a total of 129,024 fits. When the different analyses are combined into a histogram to determine the systematic error, the results from different fitting functions or lattice spacing cuts are weighted with the Akaike information criterion and the rest with flat weighting. We obtain:

$$w_0 = 0.17236(29)_{\rm stat}(63)_{\rm syst}(70)_{\rm tot}\ \ {\rm fm}, \tag{7}$$

where the first error is statistical, the second is systematic and the third is the total error; we reach a relative precision of 0.4%. The splitting up of the error into different sources is explained in Supplementary Information. In Extended Data Fig. 5 we show the various isospin components of $w_0 M_\Omega$ versus the lattice spacing squared, together with the different continuum extrapolations. Our result (equation (7)) is in good agreement with earlier four-flavour determinations: $w_0 = 0.1715(9)$ fm from ref. [13] and $w_0 = 0.1714^{+15}_{-12}$ fm from ref. [37]. In those studies, the isospin-symmetry-breaking effects were only estimated, whereas in our case they are fully accounted for.

The same procedure is used for $M_{ss}$. We work with $(M_{ss}/M_\Omega)^2$ instead of $M_{ss}/M_\Omega$, because the fit qualities are much better in the first case. The 129,024 different fits give:

$$M_{ss} = 689.89(28)_{\rm stat}(40)_{\rm syst}(49)_{\rm tot}\ {\rm MeV}. \tag{8}$$

Finally, we carry out the analysis for $\Delta M^2/M_\Omega^2$ with $\Delta M^2 = M_{dd}^2 - M_{uu}^2$, which is a measure of the strong–isospin breaking. Altogether we have 3,328 fits, which give the following central value with statistical, systematic and total errors:

$$\Delta M^2 = 13{,}170(320)_{\rm stat}(270)_{\rm syst}(420)_{\rm tot}\ {\rm MeV}^2. \tag{9}$$

## Data availability

The datasets used for the figures and tables are available from the corresponding author on request.

## Code availability

A CPU code for configuration production and measurements can be obtained from the corresponding author upon request. The Wilson flow evolution code, which was used to determine $w_0$, can be downloaded from https://arxiv.org/abs/1203.4469.

35. Giusti, D., Sanfilippo, F. & Simula, S. Light-quark contribution to the leading hadronic vacuum polarization term of the muon $g-2$ from twisted-mass fermions. *Phys. Rev. D* **98**, 114504 (2018).

36. Shintani, E. et al. Hadronic vacuum polarization contribution to the muon $g-2$ with 2+1 flavor lattice QCD on a larger than (10 fm)$^4$ lattice at the physical point. *Phys. Rev. D* **100**, 034517 (2019).

37. Bazavov, A. et al. Gradient flow and scale setting on MILC HISQ ensembles. *Phys. Rev. D* **93**, 094510 (2016).

**Acknowledgements** We thank J. Charles, A. El-Khadra, M. Hoferichter, F. Jegerlehner, C. Lehner, M. Knecht, A. Kronfeld, E. de Rafael and participants of the online workshop 'The hadronic vacuum polarization from lattice QCD at high precision' (16–20 November 2020) for discussions. We thank J. Bailey, W. Lee and S. Sharpe for correspondence on staggered XPT. Special thanks to A. Keshavarzi for cross-section data and discussions, and to G. Colangelo and H. Meyer for constructive criticism. The computations were performed on JUQUEEN, JURECA, JUWELS and QPACE at Forschungszentrum Jülich, on SuperMUC and SuperMUC-NG at Leibniz Supercomputing Centre in Munich, on Hazel Hen and HAWK at the High Performance Computing Center in Stuttgart, on Turing and Jean Zay at CNRS IDRIS, on Joliot-Curie at CEA TGCC, on Marconi in Rome and on GPU clusters in Wuppertal and Budapest. We thank the Gauss Centre for Supercomputing, PRACE and GENCI (grant 52275) for awarding us computer time on these machines. This project was partially funded by DFG grant SFB/TR55, by BMBF grant 05P18PXFCA, by the Hungarian National Research, Development and Innovation Office grant KKP126769 and by the Excellence Initiative of Aix-Marseille University - A*MIDEX, a French "Investissements d'Avenir" programme, through grants AMX-18-ACE-005, AMX-19-IET-008 - IPhU and ANR-11-LABX-0060.

**Author contributions** S.B., K.K.S. and B.C.T. wrote the codes and carried out the runs for configuration generation and measurements. S.B., Z.F., K.K.S., B.C.T. and L.V. were the main developers of the scale setting; L.L., K.K.S. and B.C.T. of the isospin breaking; F.S., K.K.S. and B.C.T. of the XPT; L.L., F.S. and C.T. of the MLLGS model; L.L., K.K.S. and B.C.T. of the RHO model; S.B., Z.F. and K.K.S. of the lattice finite-size study; K.K.S. and C.T. of the finite-size effects of isospin breaking; C.H., K.K.S. and B.C.T. of the overlap simulations. The global analysis strategy was developed by S.B., Z.F., S.D.K., L.L., F.S., K.K.S. and B.C.T. The global fits were carried out by S.B., J.N.G., S.D.K. and B.C.T. R-ratio and perturbative computations were done by Z.F., L.L., K.K.S. and C.T. Various crosschecks were performed by K.M., L.P., B.C.T. and C.T. S.B., Z.F., L.L., T.L. and K.K.S. were involved in acquisition of computer resources. Z.F., L.L. and K.K.S. wrote the main paper. Z.F. and K.K.S. coordinated the project.

**Competing interests** The authors declare no competing interests.

**Additional information**
**Supplementary information** The online version contains supplementary material available at https://doi.org/10.1038/s41586-021-03418-1.
**Correspondence and requests for materials** should be addressed to Z.F.
**Peer review information** *Nature* thanks Gilberto Colangelo, Harvey Meyer and the other, anonymous, reviewer(s) for their contribution to the peer review of this work.

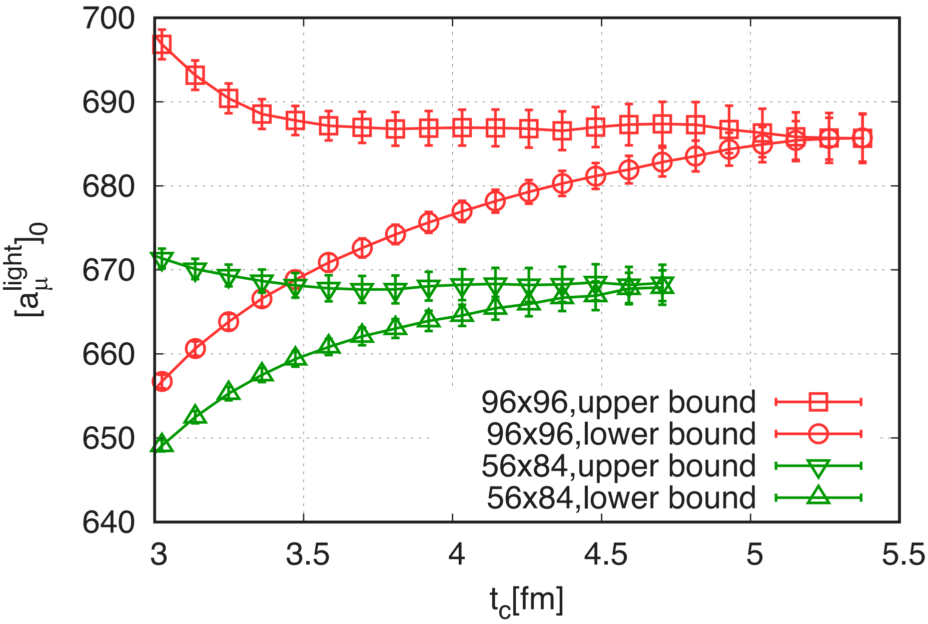


**Extended Data Fig. 1 | Upper and lower bounds on the light isospin-symmetric component of $a_\mu$, $[a_\mu^{light}]_0$.** The bounds are computed using the lattice correlator below a time separation of $t_c$ and an analytical formula describing the large-time behaviour above $t_c$.The results shown are obtained with the 4HEX action on two different lattice sizes, $56\times84$ and $96\times96$, both at $a = 0.112$ fm lattice spacing and $M_\pi = 121$ MeV Goldstone pion mass. We also carried out another simulation with $M_\pi = 104$ MeV mass. From these two, we interpolate to $M_\pi = 110$ MeV. This value ensures that a particular average of pion tastes is fixed to the physical value of the pion mass (see text). Error bars are statistical errors (s.e.m.).

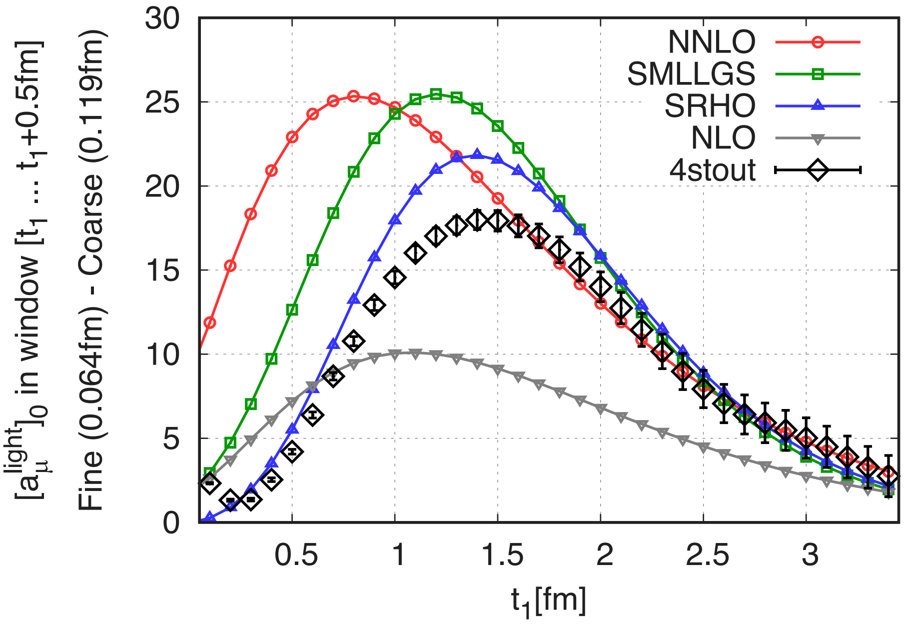


**Extended Data Fig. 2 | Isospin-symmetric component of $a_\mu^{\mathrm{light}}$, computed with a sliding window.** The window starts at $t_1$ and ends 0.5 fm later. The plot shows the difference between a fine and a coarse lattice with spacing $a$ = 0.064 fm and $a$ = 0.119 fm. The black squares with error bars are obtained from the simulation, and errors are statistical (s.e.m.). The coloured curves are the predictions of NLO, NNLO SXPT, and the SRHO and SMLLGS models. They are computed at the parameters (pion mass, taste violation, volume) of the simulations.

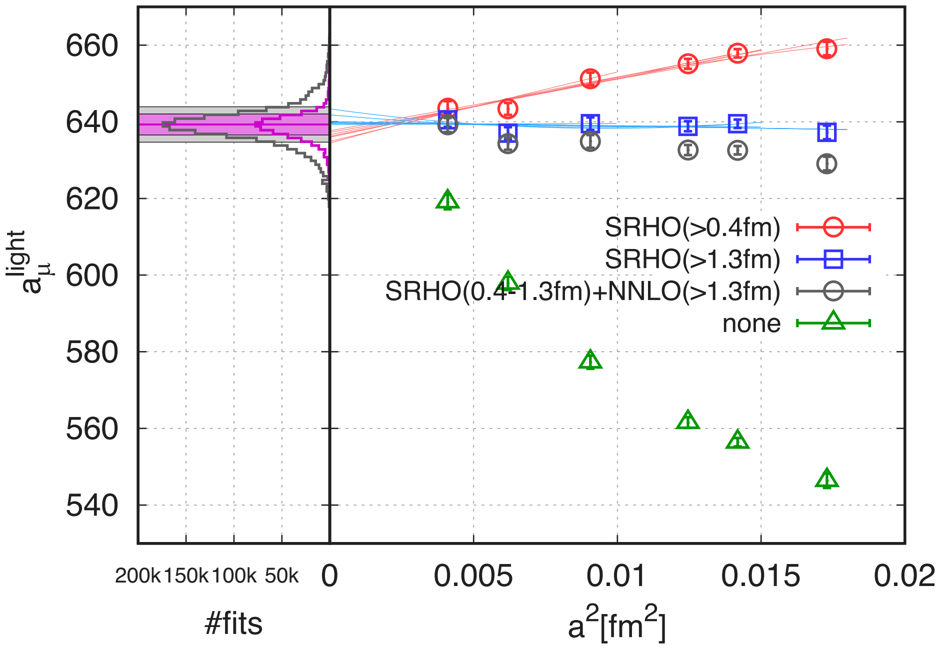


**Extended Data Fig. 3 | Example continuum limits of $a_\mu^{\mathrm{light}}$.** The light-green triangles labelled 'none' correspond to our lattice results with no taste improvement. The blue squares repesent data that have undergone no taste improvement for $t < 1.3$ fm and SRHO improvement above. The blue curves correspond to example continuum extrapolations of improved data to polynomials in $a^2$, up to and including $a^4$. We note that extrapolations in $a^2\alpha_s(1/a)^3$, with $\alpha_s(1/a)$ the strong coupling at the lattice scale, are also considered in our final result. The red circles and curves are the same as the blue points, but correspond to SRHO taste improvement for $t \geq 0.4$ fm and no improvement for smaller $t$. The purple histogram results from fits using the SRHO improvement, and the corresponding central value and error is the purple band. The darker grey circles correspond to results corrected with SRHO in the range 0.4–1.3 fm and with NNLO SXPT for larger $t$. These latter fits serve to estimate the systematic uncertainty of the SRHO improvement. The grey band includes this uncertainty, and the corresponding histogram is shown with grey. Errors are s.e.m.

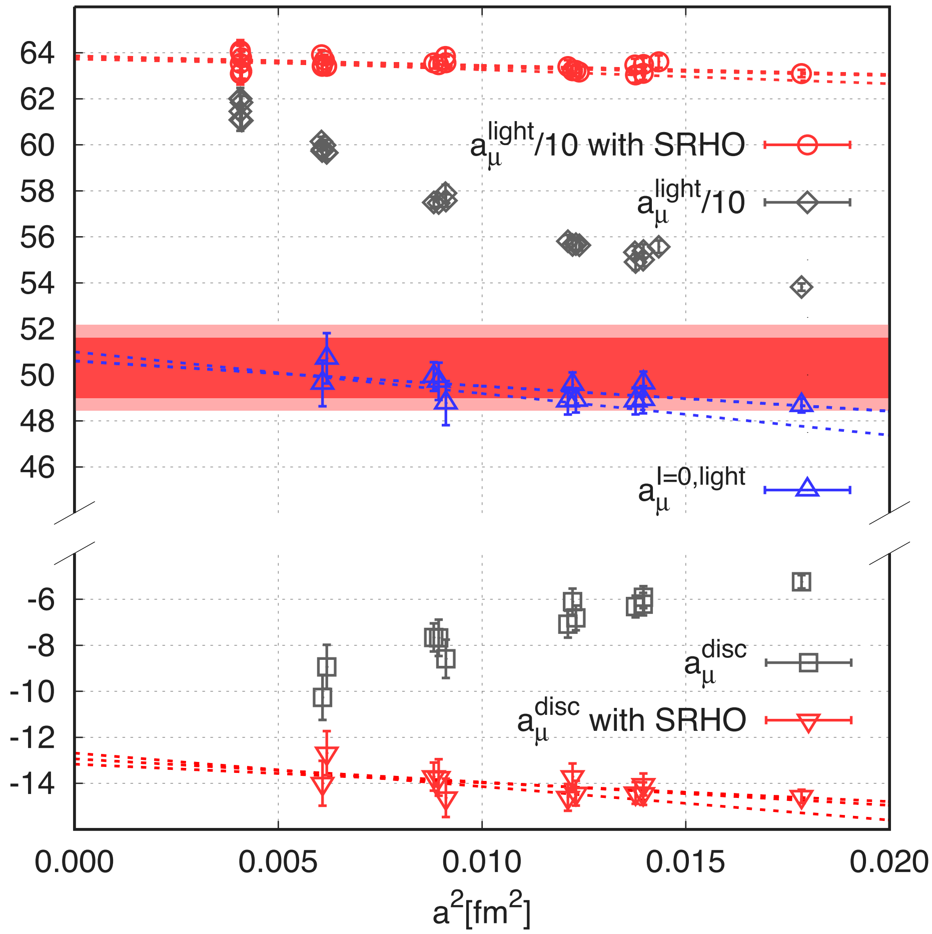


**Extended Data Fig. 4 | Comparison of the continuum extrapolation of $a_\mu^{I=0,\mathrm{light}}$ to those of $a_\mu^{\mathrm{light}}$ and $a_\mu^{\mathrm{disc}}$.** Top, grey points correspond to our uncorrected results for $\frac{1}{10}a_\mu^{\mathrm{light}}$. The red symbols show the same results with our standard SRHO taste improvement. They have a much milder continuum limit that exhibits none of the nonlinear behaviour of the grey points. The red curves show typical examples of illustrative continuum extrapolations of those points. Bottom, grey and red points and curves are the same quantities, but for $a_\mu^{\mathrm{disc}}$. Combining the results from the two individual continuum extrapolations of $\frac{1}{10}a_\mu^{\mathrm{light}}$ and $a_\mu^{\mathrm{disc}}$, according to equation (6), gives the result with statistical errors illustrated by the red band, with combined statistical and systematic errors indicated by the broader pink band. The blue points correspond to our results for $a_\mu^{I=0,\mathrm{light}}$ for each of our simulations, and are obtained by combining the two sets of grey points, according to equation (6). As these blue points show, the resulting continuum-limit behaviour of $a_\mu^{\mathrm{light}}$ is much milder than that of either the uncorrected $a_\mu^{\mathrm{light}}$ or $a_\mu^{\mathrm{disc}}$, and shows none of their curvature. This behaviour resembles much more that of the taste-improved red points. Moreover, all of the blue points, including typical continuum extrapolations drawn as blue lines, lie within the bands. This suggests that our taste improvements neither bias the central values of our continuum-extrapolated $a_\mu^{\mathrm{light}}$ and $a_\mu^{\mathrm{disc}}$, nor do they lead to an underestimate of uncertainties. Errors are s.e.m.

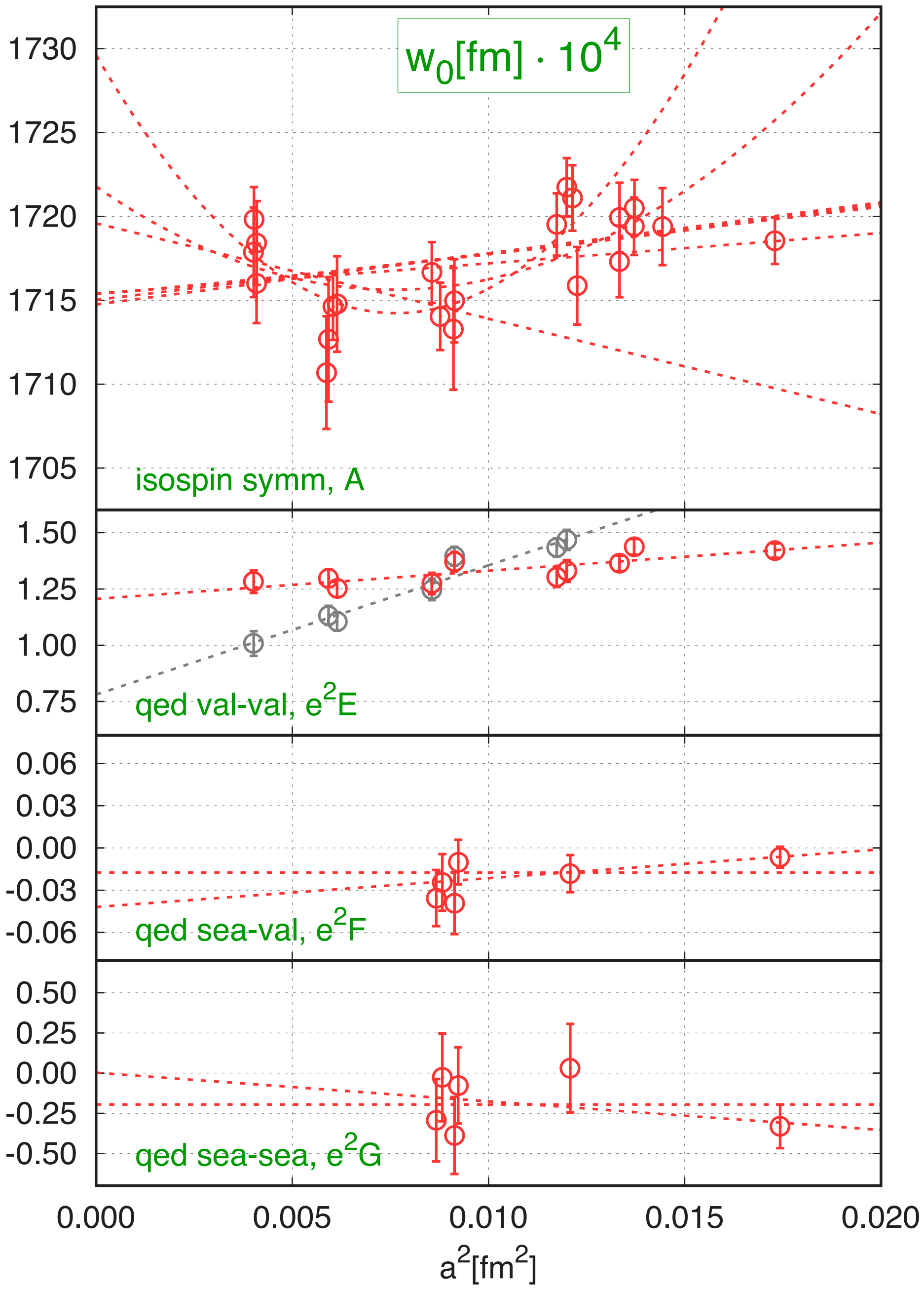


**Extended Data Fig. 5 | Continuum extrapolations of the contributions to $w_0M_\Omega$.** From top to bottom: isospin-symmetric, electromagnetic valence–valence, sea–valence and sea–sea components. The results are multiplied by $10^4/M_\Omega^*$ and the electric derivatives are multiplied by $e_*^2$, where the asterisk denotes physical value. Error bars show statistical errors (s.e.m.). Dashed lines are continuum extrapolations, showing illustrative examples from our several thousand fits. Only the lattice spacing dependence is shown: the data points are moved to the physical light- and strange-quark mass point. This adjustment varies from fit to fit, and the red data points are obtained in an $a^2$-linear fit to all ensembles. If in a fit the adjusted points differ considerably from the red points, we show them with grey colour. The final result is obtained from a weighted histogram of the several thousand fits.

**Extended Data Table 1 | Isospin-symmetric component of $a_\mu^{\mathrm{light}}$**

| $M_\pi$ in 4HEX $\rightarrow$ | 104 MeV | 121 MeV | 110 MeV |
|---|---|---|---|
| $a_\mu^{\mathrm{light}}(56 \times 84)$ | 685.9(2.7) | 668.3(2.0) | 679.5(1.9) |
| $a_\mu^{\mathrm{light}}(96 \times 96)$ | 710.7(1.9) | 684.3(1.7) | 701.1(1.3) |

The values are obtained from simulations with the 4HEX action on two different volumes and two different Goldstone pion masses. In the last column we give the interpolated value at the physical point, using the HMS averaged pion mass prescription.

**Extended Data Table 2 | Finite-size effect in the reference box of the isospin-symmetric component of $a_\mu$**

| | NLO XPT | NNLO XPT | MLLGS | HP | RHO |
|---|---|---|---|---|---|
| $a_\mu(L_{\mathrm{big}}, T_{\mathrm{big}}) - a_\mu(L_{\mathrm{ref}}, T_{\mathrm{ref}})$ | 11.6 | 15.7 | 17.8 | – | – |
| $a_\mu(L_{\mathrm{big}}, \infty) - a_\mu(L_{\mathrm{ref}}, \infty)$ | 11.2 | 15.3 | 17.4 | 16.3 | 14.8 |
| $a_\mu(\infty, \infty) - a_\mu(L_{\mathrm{big}}, T_{\mathrm{big}})$ | 0.3 | 0.6 | – | – | – |
| $a_\mu(\infty, \infty) - a_\mu(L_{\mathrm{big}}, \infty)$ | 1.2 | 1.4 | – | 1.4 | 1.4 |

The values are obtained from various model approaches.